INTERNATIONAL ATOMIC ENERGY AGENCY
UNITED NATIONS EDUCATIONAL, SCIENTIFIC AND CULTURAL ORGANIZATION

INTERNATIONAL CENTRE FOR THEORETICAL PHYSICS
34100 TRIESTE (ITALY) - P.O.B. 586 - MIRAMARE - STRADA COSTIERA 11 - TELEPHONES: 224281/2/3/4/5/6
CABLE: CENTRATOM - TELEX 460392-1

SMR/110/A - 3

WORKING PARTY

ON

"PHYSICS OF CONDENSED MATTER AT PLANETARY PRESSURES"

(20 August - 7 September 1984)

# POLYMORPHIC TRANSITIONS

## II : Mineral transitions at ultra-high pressures

A.M. THOMPSON

Dept. für Erdwissenschaften
E.T.H. Zürich, CH-8092
Switzerland

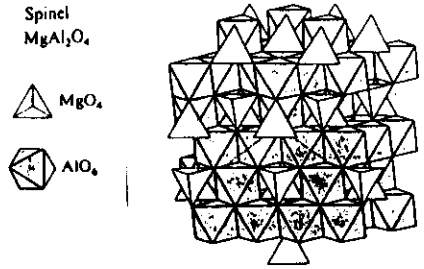


FIGURE II.97 Crystal structure of spinel.

Zoltai & Stout (1984)

TABLE II.4. *Classification of Normal and Inverse Spinel Structures*

| Mineral Name | Formula | Structure |
|---|---|---|
| Chromite | $Fe^{2+}[Cr^{3+}]_2O_4$ | N |
| Magnesiochromite | $Mg^{2+}[Cr^{3+}]_2O_4$ | N |
| Hercynite | $Fe^{2+}[Al^{3+}]_2O_4$ | N |
| Galaxite | $Mn^{2+}[Al^{3+}]_2O_4$ | N |
| Franklinite | $Zn^{2+}[Fe^{3+}]_2O_4$ | N |
| "Silicate Spinel" | $Si^{4+}[Mg^{2+}]_2O_4$ | N |
| Magnetite | $Fe^{3+}[Fe^{2+}Fe^{3+}]O_4$ | I |
| Magnesioferrite | $Fe^{3+}[Mg^{2+}Fe^{3+}]O_4$ | I |
| Jacobsite | $Fe^{3+}[Mn^{2+}Fe^{3+}]O_4$ | I |
| Spinel | $Al^{3+}[Mg^{2+}Al^{3+}]O_4$ | I |
| Ulvospinel | $Fe^{2+}[Fe^{2+}Ti^{4+}]O_4$ | I |
| "Silicate Spinel" | $Mg^{2+}[Si^{4+}Mg^{2+}]O_4$ | I |

NOTE: N = normal, I = inverse.

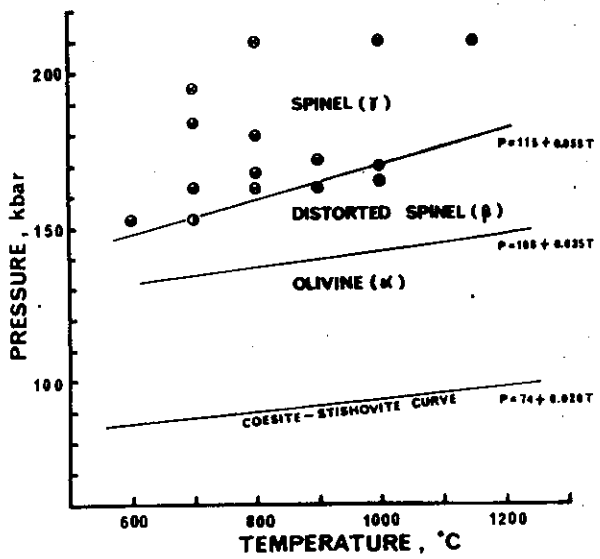


*Fig. 8. β-γ phase transition curve and the α-β phase transition curve in pure $Mg_2SiO_4$. The coesite-stishovite transition curve is also shown.*

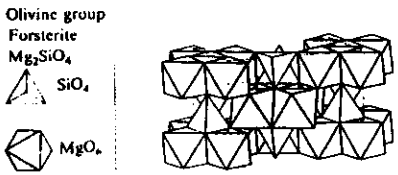


FIGURE II.51 Crystal structure of forsterite, *a* axis vertical.

Suito (1977)

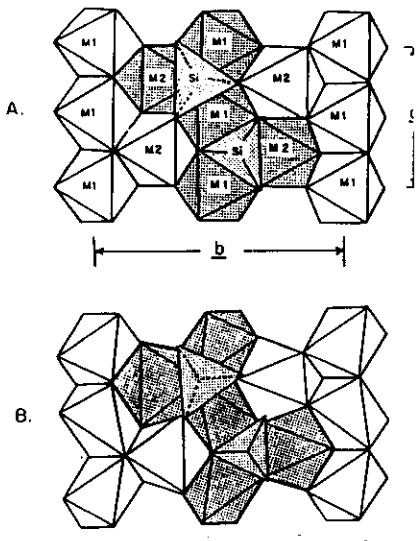


FIG. 1. Olivine crystal structure: *A*—ideal HCP model, *B*—actual structure, (after Brown, 1970).

Hazen (1977)

Crystal Structural Features of the Olivine–Spinel Transition

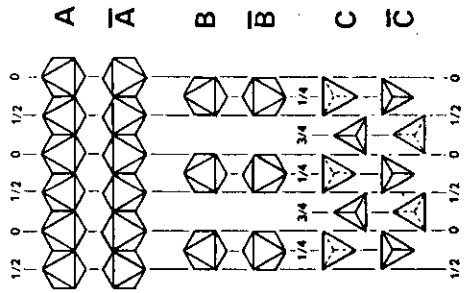


Sung & Burns (1976)

Horiuchi et al (1982)

Fig. 2. Three basic structural units for the three polymorphs, α, β, and γ. *A* Continuous octahedral chain. *B* Discontinuous octahedral row, and *C* Discontinuous tetrahedral row. The symbols *A*, *B*, *C* indicate that the polyhedral unit is overturned (mirror image). The numbers 0, 1/4, 1/2, and 3/4 refer to the fractional translation of a unit cell distance

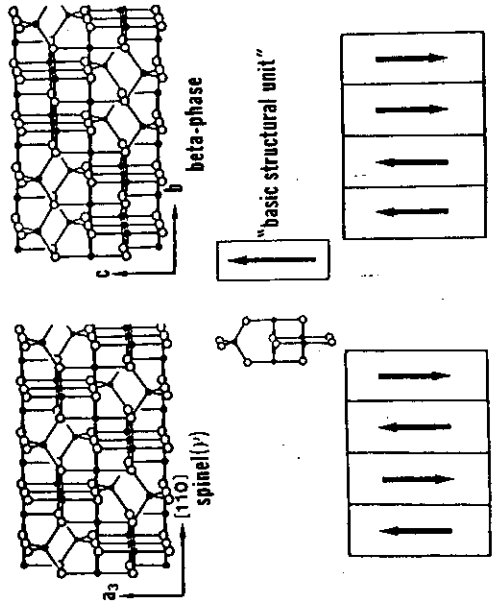


Fig. 5. Perspective views of spinel and β-phase structures (top), basic structural unit (middle), and the arrangements of basic structural unit in spinel and β-phase structures (bottom). Perspective views are from MORIMOTO *et al.* (1969).

C. M. Sung and R. G. Burns

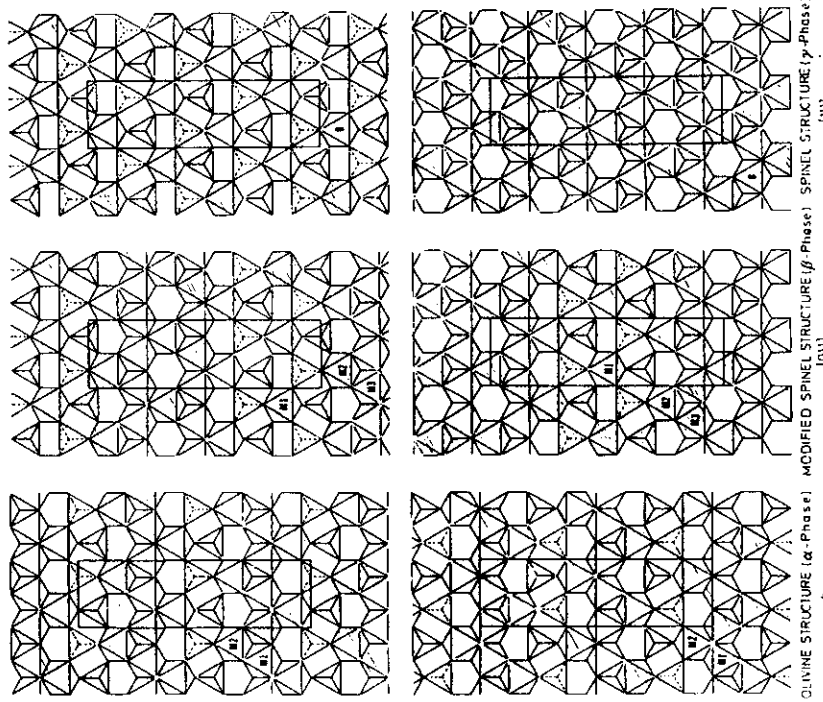


Fig. 1. Schematic diagram showing the different linkages of occupied polyhedral layers in the three polymorphs. The closest packed layers of oxygen atoms are parallel to the plane of the paper. Octahedra (*M*) and tetrahedra (*T*) are cross-hatched and stippled respectively. (*A*) α structure projected onto (100); (*B*) β structure projected onto (011); (*C*) γ structure projected onto (111). For each structure, the upper polyhedral layer lies directly above the lower one. The projected unit cells are outlined and they contain 2, 6, and 6 polyhedral layers for the α, β, and γ structures, respectively. The specific *M*-sites for the three structures are also labelled (modified after Morimoto *et al.*, 1974)

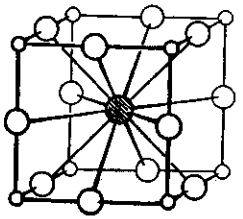

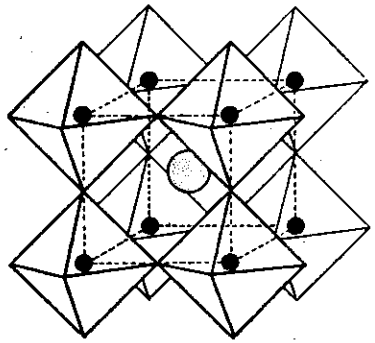

Ringwood (1975)

FIGURE 12-12
The idealized structure of perovskite $CaTiO_3$. A Ca atom is at the cube centre, and the Ti-O octahedra are shown diagrammatically. (*After Naray-Szabo, 1943.*)

FIGURE 12-1
Phases observed in the system $FeSiO_3$-$MgSiO_3$ at pressures up to 200 kbars at approximately 1000°C. Symbols as follows:

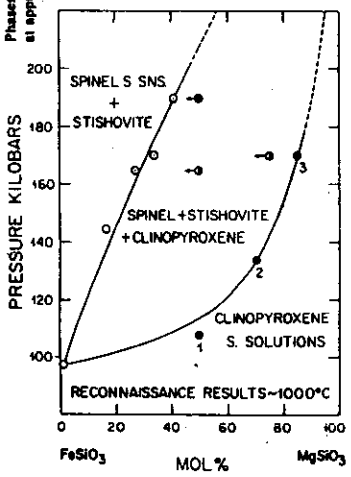


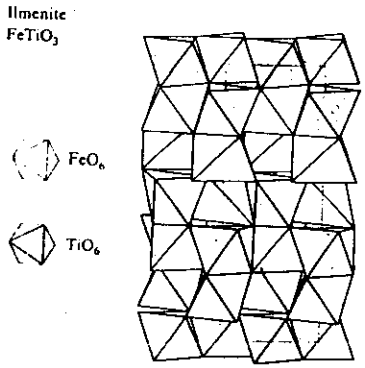


FIGURE II.92 Crystal structure of ilmenite, *c* axis vertical.

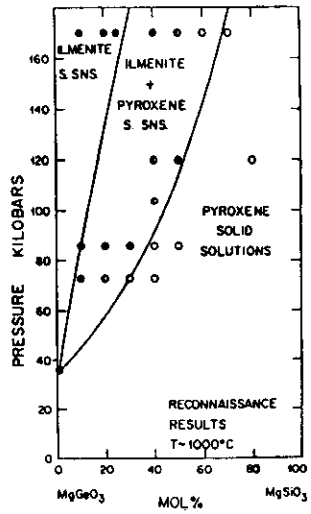


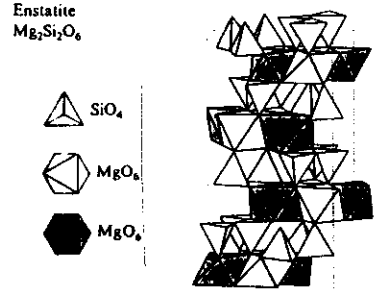


FIGURE II.33 Crystal structure of enstatite, *a* axis vertical.

Zoltai & Stout (1984)

FIGURE 12-2
Phases present in the system $MgGeO_3$-$MgSiO_3$ at pressures up to 170 kbars and at approximately 1000°C.



Table 12-2 COMPARATIVE MOLAR VOLUMES OF COMPOUNDS POSSESSING ILMENITE STRUCTURES AND FORMED FROM END-MEMBERS POSSESSING ROCKSALT AND RUTILE STRUCTURES

| Compound | Molar volume $V$ ($cm^3$) | Isochemical oxide volume $v$ ($cm^3$) | $\Delta v/v$ (%)* |
|---|---|---|---|
| $CdTiO_3$ | 35.69 | 30.39 | 3.8 |
| $CoTiO_3$ | 31.05 | 30.44 | 2.0 |
| $MgGeO_3$ | 29.14 | 27.91 | 4.4 |
| $MgTiO_3$ | 30.86 | 30.05 | 2.7 |
| $MnGeO_3$ | 31.28 | 29.88 | 4.7 |
| $MnTiO_3$ | 32.76 | 32.02 | 2.3 |
| $MnVO_3$ | 32.01 | 31.10 | 2.9 |
| $FeTiO_3$ | 31.69 | 30.84 | 2.8 |
| $NiTiO_3$ | 30.56 | 29.77 | 2.7 |
| $NiMnO_3$ | 28.42 | 27.58 | 3.0 |
| $CoMnO_3$ | 29.43 | 28.25 | 4.2 |
| $MgSiO_3$ | 26.40 | 25.26 | 4.5 (assumed) |
| $FeSiO_3$† | 24.87 | 23.91 | 4.0 (assumed) |

*$\Delta v = V - v$.
†$Fe^{++}$ in low-spin configuration with radius of 0.61 Å (Shannon and Prewitt, 1969).

Ringwood(1975)

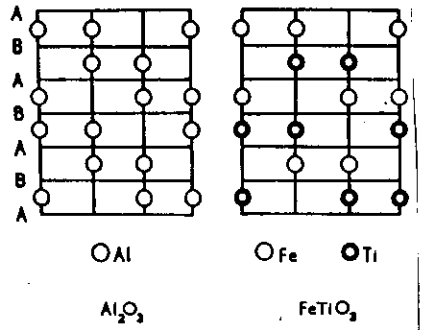


FIGURE 12-3
Diagrammatic comparison of the distribution of metal atoms in corundum and ilmenite. The structures are viewed on (2$\bar{1}$$\bar{1}$0). Horizontal lines A, B indicate the positions of the close-packed layers of oxygen atoms. (*From Wells, 1962, with permission. Copyright Oxford University Press. By permission of the Clarendon Press, Oxford.*)

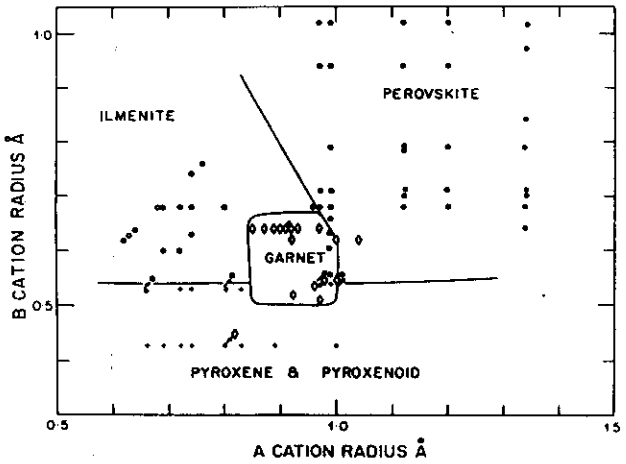


FIGURE 12-4
Plot of A and B ionic radii for $A^{++}B^{4+}O_3$ compounds possessing pyroxene, ilmenite, perovskite, and garnet structures and for $A_3^{++}B_2^{4+}O_{12}$ garnets. Arrows indicate high-pressure transformations. (*From Ringwood, 1970, with permission.*)

Zoltai & Stout (1984)

Garnet group
Grossular
$Ca_3Al_2Si_3O_{12}$

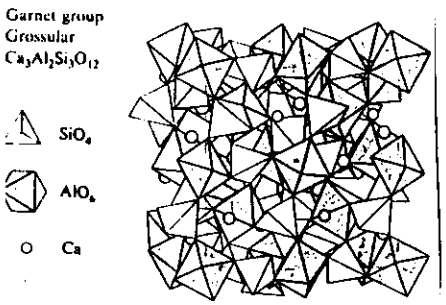


FIGURE II.50 Crystal structure of grossular, a garnet.

Ringwood (1975)

Table 12-3 STRUCTURAL FORMULAE, IONIC SUBSTITUTIONS, AND EXAMPLES OF GARNETS*

$A_3^{VIII}B_2^{VI}C_3^{IV}O_{12}$
$A_3^{VIII}C_2^{VI}C_3^{IV}O_{12}$
$A_2^{VIII}(AC)^{VI}C_3^{IV}O_{12}$

| | | | Examples |
|---|---|---|---|
| A cations | + | Na, K | $Mg_3Al_2Si_3O_{12}$ |
| | ++ | Ca, Mg, Fe, Mn, Cd, Co, Cu, Zn, Sr, Ba, Mn | $Ca_3(TiMg)Si_3O_{12}$ |
| | 3+ | Rare earths, Bi, Y | $(CdGd_2)Mn_2Ge_3O_{12}$ |
| | 4+ | Zr, Hf | $(NaCa_2)Ni_2V_3O_{12}$ |
| | | | $Na_3Al_2Li_3F_{12}$ |
| | | | $(CaNa_2)Ti_2Si_3O_{12}$ |
| | | | $Y_3Al_2Al_3O_{12}$ |
| | | | $Ca_3(CaGe)Ge_3O_{12}$ |
| | | | $Mn_3(MnSi)Si_3O_{12}$ |
| | | | $(NaCa_2)Mg_2P_3O_{12}$ |
| | | | $(Na_2Ca)Si_2Si_3O_{12}$ |
| B cations | + | Li | |
| | ++ | Mn, Co, Mg, Ni, Zn, Fe, Ca, Cd | |
| | 3+ | Fe, Ga, Al, Cr, V, Sc, In, Rh, Mn, Co | |
| | 4+ | Sn, Ge, Si, Ti, Zr, Hf, Ru | |
| | 5+ | Nb, Ta, Sb | |
| C cations | + | Li | |
| | ++ | Co | |
| | 3+ | Fe, Ga, Al, Co | |
| | 4+ | Si, Ge, Sn, Ti | |
| | 5+ | As, V, P | |
| Anions | | $O^{--}$, $F^-$, $OH^-$ | |

*General references: Wyckoff (1965), Geller (1967).

Ito & Matsui (1977)

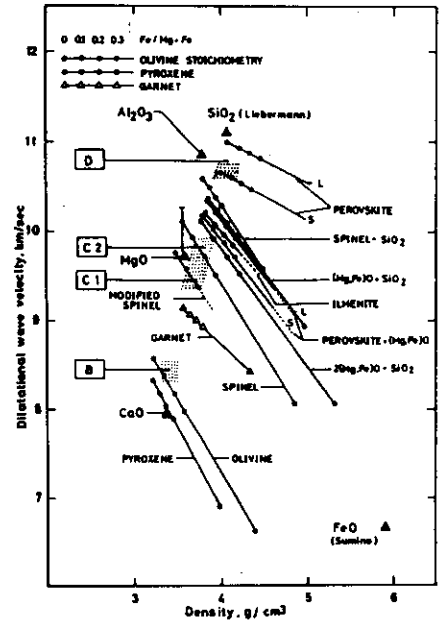


*Fig. 6. The Vp–ρ plots for mantle candidate phases and the mantle materials at ambient condition. Perovskite L, Liu [1976a]; Perovskite S, present work; FeO, Sumino [unpublished]; $SiO_2$, Liebermann [in press 1976]. See text for detail.*



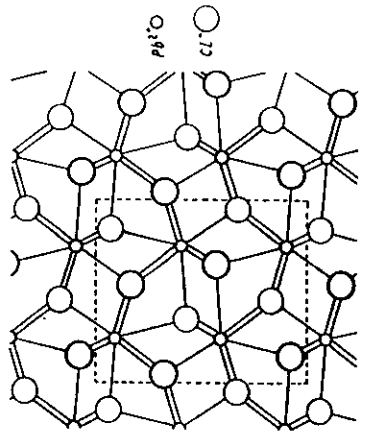


FIG. 98. Projection of the crystal structure of $PbCl_2$ on (100).

Atoms at heights a/4 and 3a/4 above the plane of the paper are distinguished as heavy and light circles.

Wells (1962)

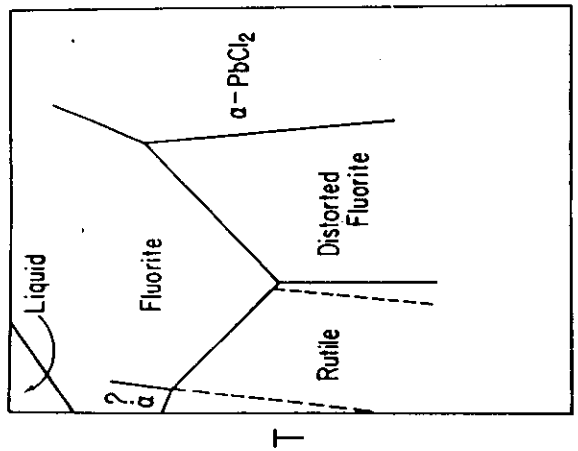


Jamieson (1977)

*Fig. 2. "Rubber" phase diagram for $AX_2$ compounds showing availability of large possible $\Delta V/V_o$ for phase transitions from the rutile type.*

Zoltai & Stout (1984)

Wells (1962)

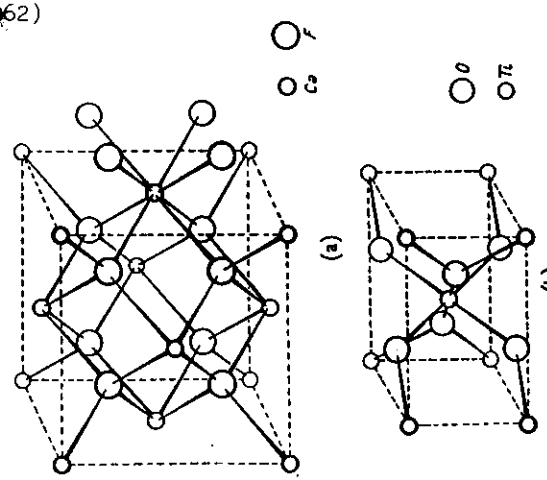


FIG. 18. The fluorite ($CaF_2$) and rutile ($TiO_2$) structures.

Rutile
$TiO_2$

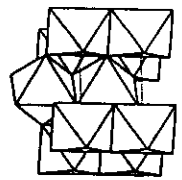

FIGURE II.93 Crystal structure of rutile, c axis vertical.

Ringwood (1975)

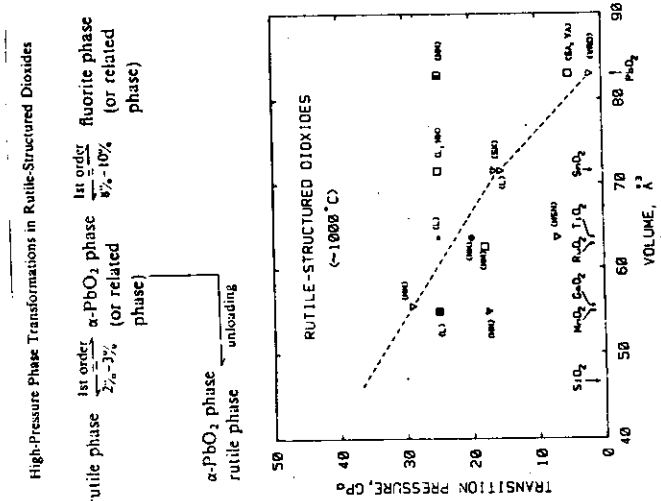


Fig. 9. A plot of phase transformation pressure *vs.* the unit cell volume (Å³) for rutile-structured dioxides at 1,000°C where the symbol ▽ is for rutile phase ⇌ α-$PbO_2$ phase or its related phase, ▼ for rutile phase ⇌ orthorhombic phase, □ for α-$PbO_2$ ⇌ fluorite phase, ■ for fluorite ⇌ tetragonal phase, ◆ for α-$PbO_2$ phase ⇌ orthorhombic phase, * for α-$PbO_2$ phase ⇌ hexagonal phase, and ■ for rutile ⇌ cubic phase. All the unit cell volume data for rutile phases are taken from Baur and Khan (1971), L stands for Liu (1974, 1976, 1978); MM for Ming and Manghnani, this study; MSN for Manmont *et al.* (1980); SA for Syono and Akimoto (1968); SK for Sumo and Kawai (1975); WDR for White *et al.* (1961); YA for Yagi and Akimoto (1980). Hexagonal phases ($Fe_2N$ type) of $GeO_2$ and $SiO_2$ obtained from the glassy starting material (Liu *et al.*, 1978) are not included in this diagram.

Table 11-6 DENSE $A_2BO_4$ COMPOUNDS. FORMULA VOLUMES, Å³.
*(From Reid and Ringwood, 1970)*

| Compound | V(Å³) | Vol. compound (V)/ Vol. oxides ($V_o$) |
|---|---|---|
| 1. Olivine (α) type | | |
| $Ni_2SiO_4$ | 70.58 | 1.186 |
| $Mg_2SiO_4$ | 72.68 | 1.199 |
| $Co_2SiO_4$ | 73.96 | 1.191 |
| $Mg_2GeO_4$ | 76.34 | 1.175 |
| $Fe_2SiO_4$ | 76.81 | 1.206 |
| $Mn_2SiO_4$ | 80.70 | 1.201 |
| $MgMnGeO_4$ | 81.29 | 1.191 |
| $CoMnGeO_4$ | 81.72 | 1.185 |
| $FeMnGeO_4$ | 82.76 | 1.186 |
| $Mn_2GeO_4$ | 84.84 | 1.186 |
| $CaMgSiO_4$ | 85.27 | 1.222 |
| γ-$Ca_2SiO_4$ | 96.75 | 1.226 |
| $Ca_2GeO_4$ | 102.0 | 1.226 |
| 2. β-$Mg_2SiO_4$ type | | |
| $Mg_2SiO_4$* | 67.41 | 1.112 |
| $Co_2SiO_4$* | 69.08 | 1.112 |
| $Mn_2GeO_4$* | 79.72 | 1.115 |
| $Zn_2SiO_4$* | 69.29 | |

*High-pressure phases.
†$V$ is the volume per formula unit. $V_o$ is the sum of the formula volumes of the constituent oxides of rocksalt, rutile, or corundum type.

Wells (1962)

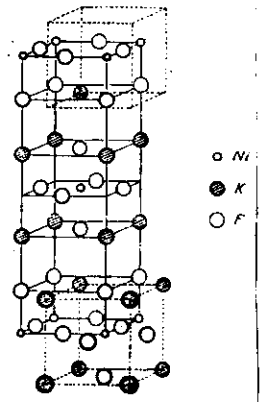


FIG. 166. The $K_2NiF_4$ structure.

Table 11-6 (*continued*)

| | V(Å³) | V/V_o† |
|---|---|---|
| 3. $A_2BO_4$ spinel (γ) type | | |
| $Ni_2SiO_4$* | 65.04 | 1.093 |
| $Co_2SiO_4$* | 67.37 | 1.085 |
| $Ni_2GeO_4$ | 69.45 | 1.088 |
| $Fe_2SiO_4$* | 69.78 | 1.096 |
| $Mg_2GeO_4$ | 70.09 | 1.079 |
| $Li_2NiF_4$ | 71.81 | 1.092 |
| $Co_2GeO_4$ | 71.94 | 1.083 |
| $NiMnGeO_4$* | 73.03 | 1.079 |
| $Mg_2VO_4$ | 73.71 | 1.103 |
| $Fe_2GeO_4$ | 74.38 | 1.094 |
| $CoMnGeO_4$* | 74.78 | 1.084 |
| $Co_2TiO_4$ | 75.13 | 1.073 |
| $Mg_2TiO_4$ | 75.15 | 1.096 |
| $FeMnGeO_4$* | 75.90 | 1.088 |
| $Fe_2TiO_4$ | 77.74 | 1.085 |
| $Mg_2SnO_4$ | 80.59 | 1.103 |
| $Co_2SnO_4$ | 80.73 | 1.082 |
| 4. $Sr_2PbO_4$ (δ) type | | |
| $FeMnGeO_4$* | 70.21 | 1.006 |
| $Mn_2GeO_4$* | 71.90 | 1.005 |
| $Mn_2SnO_4$ | 80.63 | 1.012 |
| $Na_2CuF_4$‖ | 85.28 | 1.022 |
| $Cd_2SnO_4$ | 87.85 | 1.004 |
| $Ca_2SnO_4$ | 90.95 | 0.995 |
| $Ca_2PbO_4$ | 96.00 | 0.990 |
| $Sr_2PbO_4$ | 108.30 | 0.984 |
| 5. $CaMn_2O_4$ type | | |
| $Mn_3O_4$* | 70.93 | 0.979 |
| $CaMn_2O_4$ | 77.00 | 0.984 |
| 6. $K_2NiF_4$ type | | |
| $Ca_2GeO_4$* | 81.30 | 0.976 |
| $Ca_2MnO_4$ | 81.35 | 0.975 |
| $Sr_2TiO_4$ | 94.85 | 0.949 |
| $Sr_2RuO_4$ | 95.38 | 0.951 |
| $Sr_2IrO_4$ | 97.74 | 0.972 |
| $Sr_2MoO_4$ | 98.64 | 0.970 |
| $Sr_2SnO_4$ | 102.10 | 0.978 |
| $K_2NiF_4$ | 104.92 | 0.956 |
| $K_2MgF_4$ | 107.20 | 0.982 |
| $Ba_2SnO_4$ | 113.95 | 0.950 |
| $Ba_2PbO_4$ | 123.0 | 0.980 |
| 7. $CaFe_2O_4$ type | | |
| $CaAl_2O_4$* | 66.03 | 0.939 |
| β-$CaCr_2O_4$ | 71.90 | 0.944 |
| $CaV_2O_4$ | 73.80 | 0.953 |
| $CaFe_2O_4$ | 74.55 | 0.954 |
| $CaIn_2O_4$ | 87.45 | 0.962 |
| 8. $CaTi_2O_4$ | 76.08 | 0.951 |
| 9. $Ca_2IrO_4$ | 81.90 | 0.935 |

*High-pressure phases.
†$V$ is the volume per formula unit, $V_o$ the sum of the formula volumes of the constituent oxides of rocksalt, rutile, or corundum type.
‖Monoclinic distortion of $Sr_2PbO_4$ type.

Ringwood (1975)

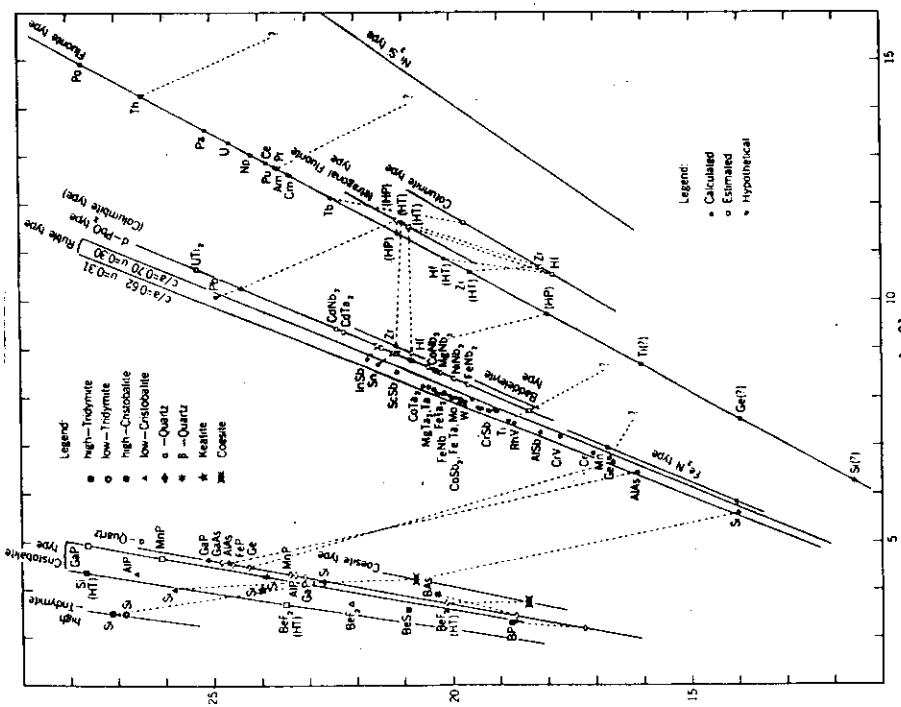


ig. 1. The molar volume for $MO_2$ (including $MNO_4$ and $MN_2O_4$) compounds possessing the tridymite, cristobalite, α-quartz, coesite, rutile, $Fe_2N$, α-$PbO_2$, baddeleyite, fluorite (tetragonal and cubic), and cotunnite types is plotted against the cube of the M-O distance. All solid lines are calculated by Liu (1981). High-pressure phase transformations are indicated by the dotted lines. Solid and open symbols are described in the text. All data are for room temperature

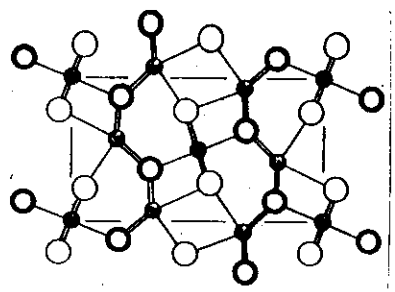

FIGURE 11-10
The structure of δ-$Mn_2GeO_4$ ($Sr_2PbO_4$ type) in projection onto (001). Small black circles, Ge; stippled circles, Mn; largest circles, oxygen appearing at two levels. *(From Wadsley, Reid, and Ringwood, 1968, with permission.)*

Table 11-7 RELATIVE VOLUMES OF $A_2BO_4$ POLYMORPHS. (*From Reid and Ringwood, 1970*)

| Structure type | Examples, with coordination numbers,* of metals and anions | $V/V_s$† | $\Delta V/V_s$(%)‡ |
|---|---|---|---|
| Olivine [$\alpha$] | $^{[6]}Mg_2{}^{[4]}Si^{[4]}O_4$ | 1.20 | 20 |
| $\beta$-$Mg_2SiO_4$ type | $^{[6]}Co_2{}^{[4]}Si_2{}^{[4]}O_4{}^{[6]}O_1{}^{[3]}O_1$ | 1.11§ | 11.5 |
| Spinel $A_2BO_4$[$\gamma$] | $^{[4]}Fe_2{}^{[4]}Si^{[4]}O_4$ | 1.09 | 9 |
| Spinel $AB_2O_4$ | $^{[4]}Mg^{[6]}Al_2{}^{[4]}O_4$ | 1.07§ | 7.5 |
| $2AO + BO_2$ | $2^{[6]}Mg^{[6]}O + {}^{[6]}Ti^{[6]}O_2$ | 1.00 | 0 |
| $AO + B_2O_3$ | $^{[6]}Mg^{[6]}O + {}^{[6]}Al_2{}^{[4]}O_3$ | 1.00 | 0 |
| $Sr_2PbO_4$ [$\delta$] | $^{[6]}Mn_2{}^{[6]}Ge^{[6]}O_4{}^{[4]}O_4$ | 1.00 | 0 |
| $CaMn_2O_4$ | $^{[8]}Ca^{[6]}Mn_2{}^{[6]}O_4{}^{[4]}O_1{}^{[4]}O_1$ | 0.98 | − 2 |
| Defect NiAs§ | $^{[6]}Fe^{[6]}Cr_2{}^{[6]}S_2{}^{[4]}S_2$ | 0.98 | − 2 |
| $K_2NiF_4$ | $^{[9]}Ca_2{}^{[6]}Ge^{[6]}O_4$ | 0.96§ | − 3.5 |
| $CaFe_2O_4$ | $^{[8]}Ca^{[6]}Al_2{}^{[4]}O_4$ | 0.94§ | − 5.5 |
| $CaTi_2O_4$ | $^{[8]}Ca^{[6]}Ti_2{}^{[6]}O_4{}^{[4]}O_1{}^{[4]}O_1$ | 0.94§ | − 5.5 |
| $Ca_2IrO_4$ | $^{[9]}Ca_2{}^{[8]}Ca_2{}^{[6]}Ca_1{}^{[6]}Ir_2{}^{[6]}O_4{}^{[6]}O_8$ | 0.93§ | − 6.5 |

*Coordination number given by superscripts in brackets.
†Structure volumes relative to sum of constituent oxide volumes, averaged from Fig. 11-14.
‡$\Delta V = V - V_s$.
§$A_2BO_4$ type not as yet obtained for oxides.

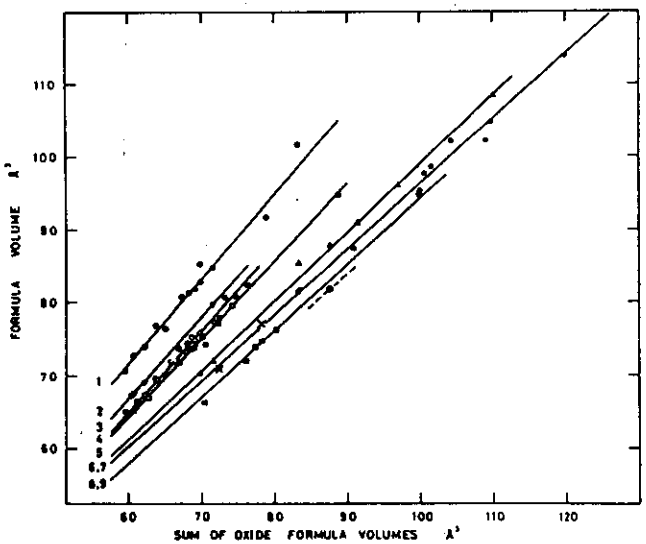


FIGURE 11-14
The formula volumes of $A_2BO_4$ and $AB_2O_4$ polymorphs versus the volumes of their isostructural mixtures of 2AX (rocksalt) + $BX_2$ (rutile) or AO (rocksalt) plus $B_2O_3$ (corundum). The structure types are shown:

1. Olivine ($\alpha$) — vertically shaded circles
2. $\beta$-$Mg_2SiO_4$ type — inverted triangles
3. $A_2BO_4$ spinel ($\gamma$) — open circles
4. $AB_2O_4$ spinel — open squares
5. $Sr_2PbO_4$ ($\delta$) — shaded triangles
6. $CaMn_2O_4$ — crosses
7. $K_2NiF_4$ — black circles
8. $CaFe_2O_4$ — shaded squares
9. $Ca_2IrO_4$ — shaded hexagon

(*From Reid and Ringwood, 1970, with permission.*)

Ringwood (1975)



Table 10-2. High-pressure transitions in silicates from $^{IV}$Si to $^{VI}$Si forms

| Formula | $^{IV}$Si Phase | $^{VI}$Si Phase | Transition Pressure | Transition $d_{Si-O}$ | Reference |
|---|---|---|---|---|---|
| $SiO_2$ | Coesite | Stishovite | 80 | 1.59 | Yagi and Akimoto (1976) |
| $Al_2SiO_5$ | Kyanite | Corundum + Stishovite | 160 | 1.60 | Liu (1974) |
| $MgSiO_3$ | Clinoenstatite | Ilmenite-type | 250 | 1.59 | Ito (1977), Liu (1977a) |
| $FeSiO_3$ | Clinoferrosilite | Wustite + Stishovite | 250 | 1.59 | Liu (1976) |
| $CaSiO_3$ | Wollastonite | Perovskite-type | 160 | 1.60 | Liu and Ringwood (1975) |
| $ZnSiO_3$ | Zinc pyroxene | Ilmenite-type | 180 | 1.59 | Liu (1977a) |
| $Mg_2SiO_4$ | Mg silicate spinel | Periclase + Perovskite-type | 270 | 1.59 | Ito (1977) |
| $Fe_2SiO_4$ | Fe silicate spinel | Wustite + Stishovite | 250 | 1.59 | Liu (1976) |
| $Ni_2SiO_4$ | Ni silicate spinel | NiO + Stishovite | 190 | 1.61 | Liu (1975a) |
| $Co_2SiO_4$ | Co silicate spinel | CoO + Stishovite | 180 | 1.61 | Liu (1975b) |
| $NaAlSi_2O_6$ | Jadeite | Calcium–Ferrite-type + Stishovite | 180 | 1.59 | Liu (1977b) |
| $KAlSi_3O_8$ | Orthoclase | Hollandite-type | 100 | 1.59 | Ringwood *et al.* (1967) |
| $Mg_3Al_2Si_3O_{12}$ | Pyrope | Ilmenite-type | 245 | 1.59 | Liu (1977c) |

Hazen & Finger (1982)

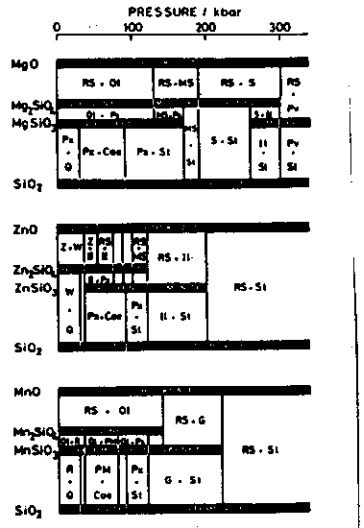


*Fig. 6. The revised Akimoto diagram showing the isothermal phase relations in the system MO-$SiO_2$ (M = Mg, Zn, Mn, Ni, Co, and Fe) at 1000°C (cf. Akimoto et al., 1976, Fig. 13). (continued)*

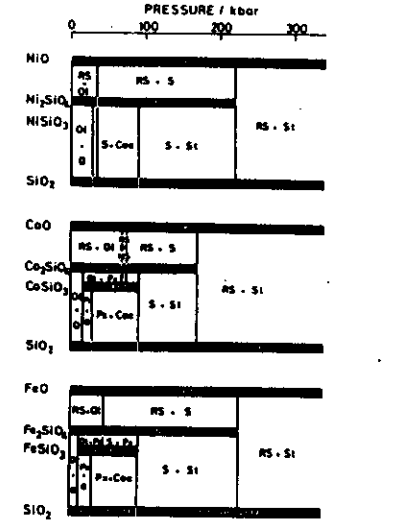


*Fig. 6 (continued)*
*Phase relations in the MgO-$SiO_2$ system above ca. 300 kbar are only schematical.*

Ito & Matsui (1977)

TABLE 1. Material Parameters for High-Pressure Ferromagnesium Silicate Phases

| | α Olivine | β Phase | γ Spinel |
|---|---|---|---|
| $V_0$ | 43.67(±0.02) + 2.6$\chi_{Fe}$ | 40.52(±0.06) + 2.7(±0.8)$\chi_{Fe}$ | 39.69(±0.01) + 2.37$\chi_{Fe}$ |
| $K_{os}$ | 129.1(±0.8) + 8.4(±0.6)$\chi_{Fe}$ | 167(±40) | 213(±4) − 16(±2)$\chi_{Fe}$ |
| $K_{os}'$ | 5.2(±0.2) | 4(±1)* | 4.8(±1) |
| $\alpha$ | 26.2 × 10$^{-6}$ | 20.6 × 10$^{-6}$* | (18.6 + 2.7$\chi_{Fe}$) × 10$^{-6}$ |
| $da/dT$ | 1.5 × 10$^{-8}$ | 1.7 × 10$^{-8}$ | 1.7 × 10$^{-8}$ |
| $\delta_s$ | 4 + 1.5$\chi_{Fe}$ | 3* | 3.5* |
| $\gamma_G$ | 1.25 | 1.3 | 1.35 |

| | Pyroxene | Garnet | Magnesiowüstite |
|---|---|---|---|
| $V_0$ | 31.33(±0.05) + 1.63(±0.03)$\chi_{Fe}$ | 113.47(±0.07) + 2.44(±0.09)$\chi_{Fe}$ | 11.25(±0.0001) + 1.00(±0.02)$\chi_{Fe}$ |
| $K_{os}$ | 108(±4) − 10(±10)$\chi_{Fe}$ | $V_0$/[0.610(±0.019) − 0.005$\chi_{Fe}$]† | 162.7(±0.2) + 17(±8)$\chi_{Fe}$ |
| $K_{os}'$ | 7(±2.5) | 4.5(±1) | 4.21(±0.14) − 0.5(±0.3)$\chi_{Fe}$ |
| $\alpha$ | 27 × 10$^{-6}$ | 18 × 10$^{-6}$ | (3.10 + 4.5$\chi_{Fe}$) × 10$^{-6}$ |
| $da/dT$ | 2.1 × 10$^{-8}$ | 1.6 × 10$^{-8}$ | 1.9 × 10$^{-8}$ |
| $\delta_s$ | 6 | 6.3 | 3 |
| $\gamma_G$ | 1.1 | 1.1 | 1.5 + 0.07$\chi_{Fe}$ |

| | Perovskite | Stishovite |
|---|---|---|
| $V_0$ | 24.46(±0.04) + 1.03(±0.28)$\chi_{Fe}$ | 14.01(±0.01) |
| $K_{os}$ | 262(±6) | 316(±10) |
| $K_{os}'$ | 4(±1)* | 4(±2) |
| $\alpha$ | 20 × 10$^{-6}$* | 16.5 × 10$^{-6}$ |
| $da/dT$ | 1.6 × 10$^{-8}$* | 10$^{-8}$ |
| $\delta_s$ | 3 | 2.5 |
| $\gamma_G$ | 1.3 | 1.7 |

$K_{os}$ is in GPa; $\alpha$ is in (°K)$^{-1}$; $da/dT$ is in (°K)$^{-2}$.
†$V_0$ is in cm$^3$/mol; assume $y$ = 0.3 [*Jeanloz and Thompson*, 1983]

Lees et al (1983)

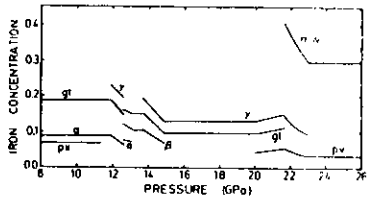


Fig. 4. Molar iron concentration ($\chi_{Fe}$ = Fe/(Fe + Mg)) versus pressure for the various phases of the olivine + garnet composition. The bulk iron content is 0.12, and the partitioning coefficients are from the references in the text. Abbreviations are as in Figures 1–3.

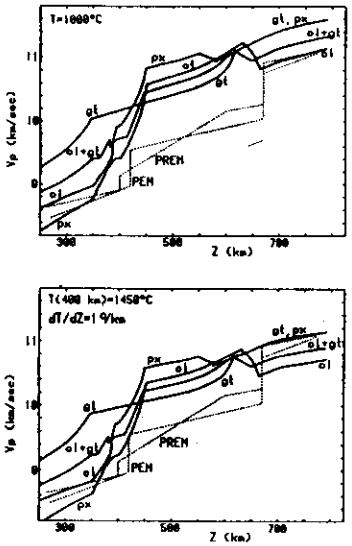


Fig. 5. Compressional velocity versus depth for the olivine, pyroxene, garnet, and olivine + garnet model mineral assemblages, for two different temperature profiles: $T$ = 1000°C and $T$(400 km) = 1450°C with $dT/dz$ = 1°/km. Compressional velocity profiles for PEM and PREM are also shown for comparison.

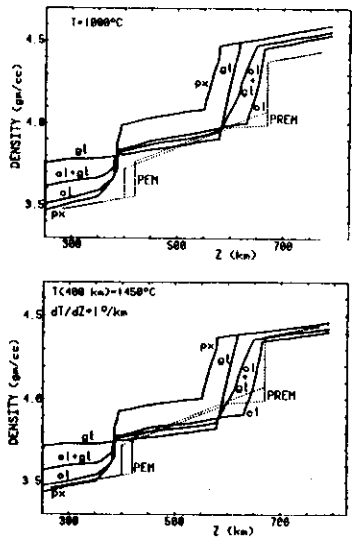


Fig. 6. Density versus depth for the olivine, pyroxene, garnet, and olivine + garnet model mineral assemblages, for two different temperature profiles: $T$ = 1000°C and $T$(400 km) = 1450°C with $dT/dz$ = 1°/km. Density profiles for PEM and PREM are also shown for comparison.



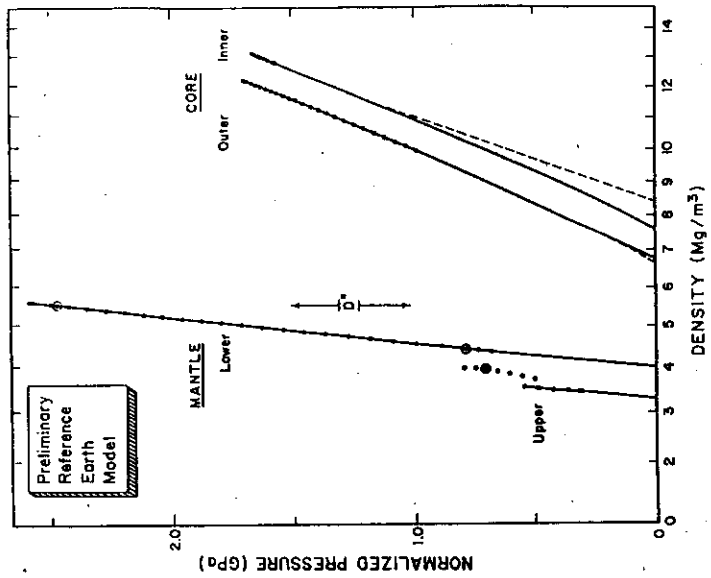


Jeanloz (1984)

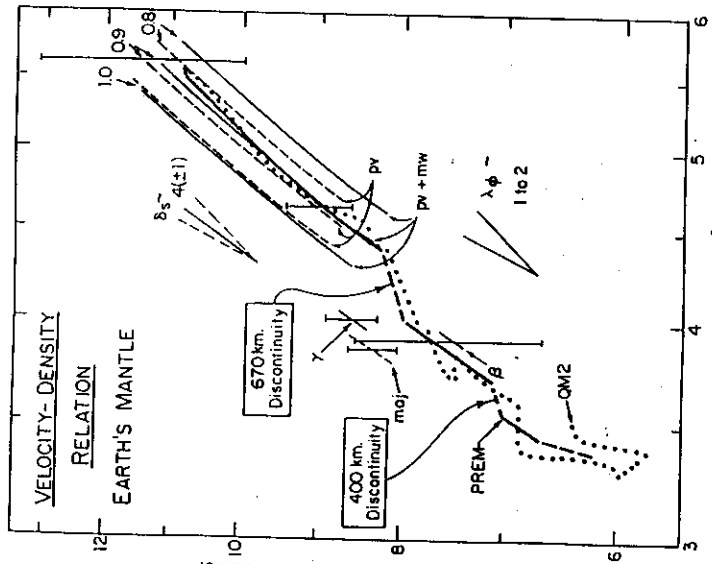


Figure 2

Jeanloz & Thompson (1983)

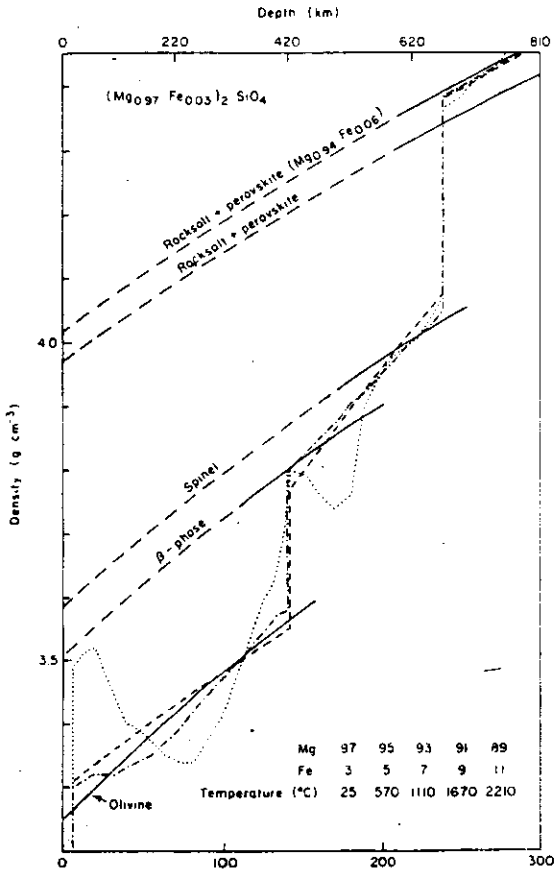


Fig. 5. Comparison of the calculated room temperature density–pressure (or depth) curves for phases of olivine, $\beta$, spinel, and the rocksalt phase plus perovskite mixture possessing an olivine stoichiometry of $(Mg_{0.97}Fe_{0.03})_2SiO_4$ with the recent density profiles of the Earth's mantle. Density–pressure curve for the mixture rocksalt plus perovskite with a stoichiometry of $(Mg_{0.94}Fe_{0.06})_2\ SiO_4$ is also displayed. Variation of the FeO/(MgO + FeO) ratio of an olivine upper mantle at c. 400 km with temperature is also listed. (After Liu, 1977*e*. — · — · —, Jordan [illegible] Anderson (1974); – – –, Dziewonski *et al.* (1975); [illegible]

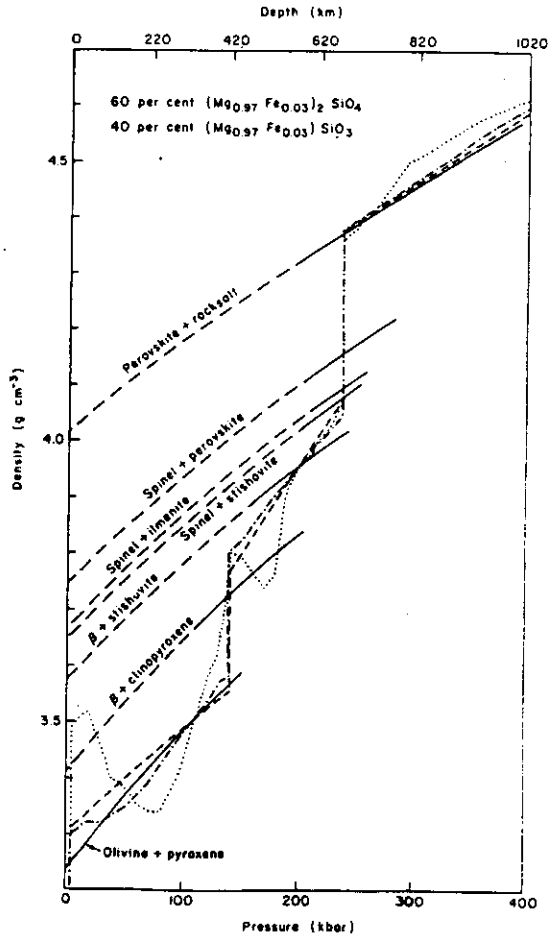


Fig. 6. Comparison of the room temperature density-pressure curves for the various phase assemblages of a mixture 60 mol per cent olivine plus 40 mol per cent pyroxene possessing the ratio FeO/(MgO + FeO) = 0.03 with the recent density profiles of the Earth's mantle above [illegible] 1000 km. (After Liu, 1977*e*.) Legend in Fig. 5.

Liu (1974) The Earth [illegible].